Journal of Structural Chemistry. Vol. 52, No. 2, pp. 340-349, 2011

STRUCTURE, THERMAL STABILITY, AND CATALYTIC PERFORMANCE OF MgO–ZrO_2 COMPOSITES

© **T. Ávalos-Rendón,[1] J. Ortíz-Landeros,[1] G. Fetter,[2] V. H. Lara,[3] P. Bosch,[1] and H. Pfeiffer[1]**

UDC 541.6:541.45

A composite constituted by zirconia supported on magnesia is thermally treated. Depending on temperature, several crystal sizes and crystalline zirconia structures are obtained. At low temperatures, cubic zirconia crystals are found to be deposited on the crystalline magnesia matrix. As temperature increases, the cubic zirconia phase transforms to the tetragonal and the monoclinic phases. They form clusters supported on the MgO matrix. All these results are supported by different analytical techniques and a catalytic test.

Keywords: catalyst supports, ceramic-matrix composites (CMCs), thermal properties, thermal analysis, zirconia.

INTRODUCTION

ZrO_2 based composites are versatile materials with conventional and advanced technological applications, including among others structural ceramics, refractories, catalysts and catalyst supports, ionic conductors, sensors or thermal barriers [1-5]. The MgO–ZrO_2 composite with a 1:1 molar ratio has been used as a solid catalyst with both acid and basic properties [6-10], as solid electrolyte for solid oxide fuel cells (SOFC) [11], as a thermal barrier coating [12, 13], and as a component of the cermet layers for the production of functionally gradient coatings [14]. Zirconia structure has to be stabilized with a second oxide since its performance is limited at high temperature. Zirconia (ZrO_2), indeed, shows polymorphism, and the associated volume cell increases by about 3-5% during martensitic transformations from tetragonal to monoclinic phase ($t \rightarrow m$) [15-18]. Thus, the design and preparation of binary oxide systems such as ZrO_2–Y_2O_3, ZrO_2–CaO, ZrO_2–CeO_2, and ZrO_2–MgO have been proposed to enhance the functionality and stability of the ZrO_2 tetragonal metastable phase [8, 19, 20].

Exhaustive investigations have found that the stability of metastable ZrO_2 phases is determined by several factors that are intimately related not only to the dopant amount and nature, but also to the composite microstructures formed. In the composite microstructures, some of the main factors that determine the stability of the phase are the morphology and distribution of zirconia inclusions into the ceramic matrix [21-24]. The aim of this paper is to study in detail the synthesis, characterization, and catalytic activity of the MgO–ZrO_2 matrix composite system, with a 1:1 molar ratio, to produce nanostructured and thermally stable ZrO_2 polymorph powders.

[1]Instituto de Investigaciones en Materiales, Universidad Nacional Autónoma de México, Circuito exterior s/n, Ciudad Universitaria, Delegación Coyoacán, CP 04510, México D.F., Mexico; pfeiffer@iim.unam.mx. [2]Facultad de Ciencias Químicas, Universidad Autónoma de Puebla, Blvd. 14 Sur y Av. San Claudio, CP 72570 Puebla, Pue., Mexico. [3]Departamento de Química, Universidad Autónoma Metropolitana-Iztapalapa, Av. Michoacán y la Purísima, Del. Iztapalapa, C.P. 09340, México D.F., Mexico. The text was submitted by the authors in English. *Zhurnal Strukturnoi Khimii*, Vol. 52, No. 2, pp. 349-357, March-April, 2011. Original article submitted September 5, 2010.

 0022-4766/11/5202-0340

EXPERIMENTAL

The MgO — 50% mol ZrO_2 composite was prepared by the coprecipitation method. Initially, magnesium carbonate ($4MgCO_3 \cdot Mg(OH)_2 \cdot nH_2O$ from Aldrich) was dissolved in a nitric acid solution (1 M). Then, zirconium acetate ($Zr(O_2C_2H_3)_4$, Aldrich) was added dropwise with continuous stirring. Once the solution was totally homogeneous, it was heated up to 70°C, to evaporate the water, under stirring. Finally, the precipitated powder was recovered, pulverized, and heat-treated at different temperatures of 400°C, 600°C, 900°C, 1000°C, and 1200°C for 8 h.

Two different XRD measurements were performed. Standard X-ray diffraction and X-ray thermo-diffraction techniques were used. In both cases, a diffractometer (Bruker AXS, D8 Advance) coupled to a copper anode X-ray tube was used. The compounds were identified by the corresponding Joint Committee Powder Diffraction Standards (JCPDS). The X-ray thermo-diffraction patterns were obtained from room temperature to 1000°C, with a temperature scanning step of 50°C, using a platinum-rhodium holder. In this case, the thermal expansion correction of the X-ray thermo-diffractograms was corrected using Pt peaks as the internal standard. The ZrO_2 interplanar distances were calculated from the thermo-diffractograms and from the standard diffractograms. Finally, the crystal size was estimated by the Scherer equation, and in those cases where it was possible, the crystallite size distribution was calculated using the XTL-SIZE program [25]. Finally, the relative content of the zirconia phases were estimated from the data obtained by XRD. The percentage of tetragonal and monoclinic phases were calculated using the integrated intensity values obtained from calculations with the WinPLOTR software, considering the diffraction peaks corresponding to (111) and $(11\bar{1})$ planes [26]. Since in all cases the chemical composition was ZrO_2, it can be assumed that X-ray absorption was the same for each phase.

Scanning and transmission electron micrographs were obtained on Cambridge Leica Stereoscan 440 and JEOL JEM-1200EX equipment respectively. For SEM analyses, the samples were previously coated with gold to avoid lack of conductivity. Samples for TEM analyses were prepared using the standard gravimetric methods.

Nitrogen adsorption-desorption isotherms were measured by a Micromeritics ASAP 2020 system at 77 K. BET surface areas were determined by the multipoint technique after thermal treatment at 400°C for 8 h in high vacuum. Finally, the differential thermal analysis (DTA) was carried out with 50 mg of sample heated from room temperature to 800°C at the rate of 10°C/min, in air atmosphere, using a TA Instruments equipment. The catalytic activity of different MgO–ZrO_2 samples was determined by acetone conversion to diacetone alcohol (DAA) through its aldolic condensation (reaction 1).

$$2CH_3{-}CO{-}CH_3 \leftrightarrow (CH_3)_2{-}C{-}(OH){-}CH_2{-}CO{-}CH_3 \quad (1)$$

All the catalytic experiments were double tested in a stirring reactor at 50°C, using 50 ml of acetone as reagent. Then, the evolution of the catalytic reaction was analyzed in a Perkin Elmer Autosystem XL chromatograph with a PE-5 capillary column (30 mm long., 0.32 mm of diameter) in the He flux. The conversion to DAA was estimated by the following equation (2):

$$X_A = \left(\frac{\frac{k_A}{k_B} A_A}{A_A + \frac{k_A}{k_B} A_B} \right) \times 100 \quad (2)$$

where, X_A is the DAA conversion at the time t, k_A and k_B are the chromatographic factors of DAA and acetone, and A_A and A_B are the areas under the DAA and acetone chromatographic peaks respectively. Still, this reaction may proceed on acid sites, producing water.

RESULTS

Figure 1 shows the XRD patterns of the powder precipitated and heat-treated at different temperatures (400°C, 600°C, 900°C, 1000°C, and 1200°C). The XRD pattern of the precipitated sample showed the formation of magnesium

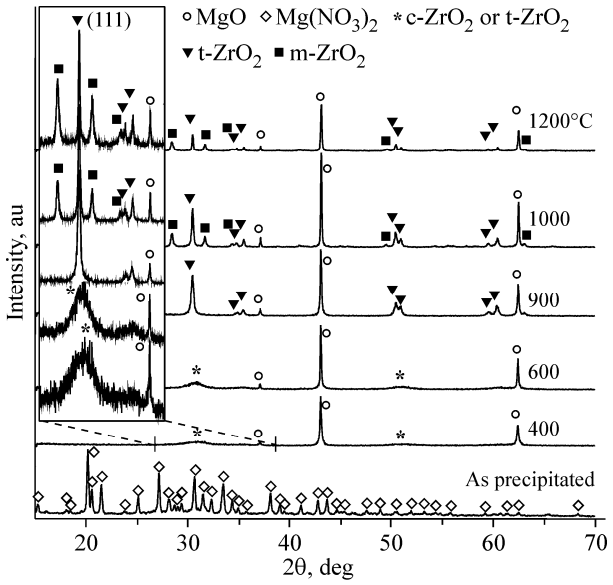

Fig. 1. XRD patterns of the MgO–ZrO_2 samples heat-treated at different temperatures. The inset shows an amplification of the XRD patterns between 27° and 39°, in 2θ.

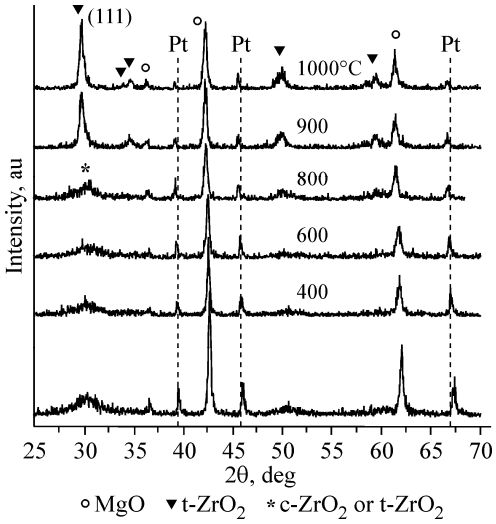

Fig. 2. X-ray thermo-diffraction patterns of MgO–ZrO_2 previously treated at different temperatures. Peaks corresponding to Pt are due to sample holder.

nitrate. Its formation is merely due to nitric acid used to dissolve magnesium carbonate. Note that no zirconium crystalline compound could be identified. Only a broad peak appears between 24° and 35° (2θ), which has to be associated to the formation of an amorphous or, more probably, a nanocrystalline phase. When the sample was heat-treated at 400°C or 600°C, magnesium nitrate peaks faded out. At 37.1°, 43.0°, and 62.4° (2θ) sharp new peaks were detected, which fitted to magnesium oxide (MgO). This result is in agreement with the magnesium nitrate decomposition temperature, which is 330°C. Actually, this compound appeared in all samples at all the other temperatures without any significant variation. Additionally, in the samples heat-treated at 400°C and 600°C, two other peaks appeared at *ca.* 29–32.5° (2θ) and 49-52° (2θ). Since they were considerably broad, it was not possible to discriminate between cubic and tetragonal ZrO_2 phases because both crystal structures present peaks almost in the same Bragg angles.

When the sample was heat-treated at 900°C, an evident change in the ZrO_2 peaks was observed. The peaks became sharper, and other new peaks appeared (34.9°, 35.47°, 59.59°, and 60.49°). These new peaks corresponded to the tetragonal ZrO_2 phase. Therefore, the ZrO_2 tetragonal phase could be assumed to occur at this temperature. Finally, at 1000°C and 1200°C the tetragonal ZrO_2 phase was detected again, but at these temperatures the monoclinic polymorph was present as well. In these cases, the monoclinic fractions calculated from the XRD data were 0.44 and 0.72 respectively. Summarizing, it seems that ZrO_2 evolves from cubic to tetragonal and later to monoclinic as a function of the annealing temperature, and the crystallinity increases as well. Of course, other experiments have to be performed in order to corroborate the presence of ZrO_2 cubic and tetragonal phases.

In order to check these results *in situ*, the sample heat-treated at 400°C was analyzed by thermo-diffraction (Fig. 2). X-ray thermo-diffraction patterns reproduce the behavior already observed by XRD. From 100°C to 800°C, ZrO_2 peaks were very broad making it impossible to distinguish between cubic and tetragonal phases. Moreover, only at 850°C ZrO_2 became more crystalline, and the tetragonal phase could be identified by the presence of the peaks at 34.9°, 35.47°, 59.59°, and 60.49°.

The only significant difference observed in the thermo-diffraction patterns is the absence of the monoclinic ZrO_2 phase at high temperatures. It can be merely explained by the fact that these experiments were performed *in situ* at high temperatures, and the monoclinic phase is stable only at temperatures lower than 1000°C, at higher temperatures the ZrO_2 stable phase is the tetragonal one.

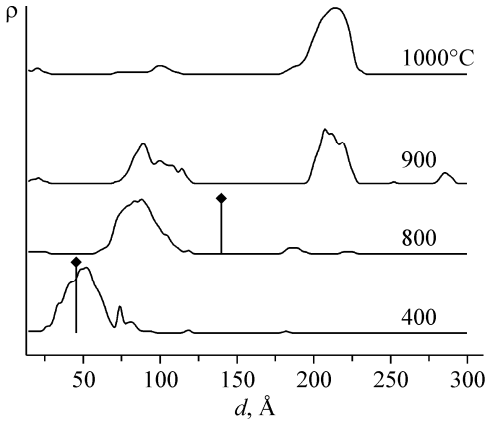

Fig. 3. Crystal size distribution of the MgO–ZrO_2 sample heat-treated at different temperatures. These measurements were obtained from the thermo-diffraction patterns. The crystal size average of the MgO–ZrO_2 sample obtained from the standard XRD are labeled as (◆).

TABLE 1. ZrO_2 Interlayer Distances Measured from the (111) Diffraction Peak of the Standard and Thermo-Diffraction XRD Patterns

Temperature (°C)	Standard diffraction	Thermo-diffraction
	Distance (Å)	Distance (Å)
400	2.897	2.944
600	2.912	2.936
900	2.934	2.986
1000	2.931	2.999
1200	2.932	—

Interplanar distances and crystallite size distributions were determined from the standard and thermo-diffraction patterns. These analyses were performed only for the ZrO_2 phase because the MgO phase is already crystalline at the beginning of the thermal process. Only some ZrO_2 interplanar distances were measured because the ZrO_2 crystalline phases are not clear and a specific crystal system cannot be proposed. In both cases, the interlayer distances of the 111 peak (29.8°) increased. In the standard diffraction patterns, the interlayer distance increased from 2.897 Å to 2.932 Å, while in the thermo-diffraction patterns, this distance increased from 2.944 Å to 2.999 Å (Table 1). These changes in the interlayer distances may be attributed to interstitial Mg-doping of the ZrO_2 phase, which should contribute to ZrO_2 tetragonal and cubic stabilization. Although the measured values were very similar in both cases, the interlayer distances were higher on the thermo-diffraction patterns. It could be attributed merely to the thermal expansion coefficient of the sample.

The crystal size calculation was also made in both systems; from the standard XRD and from the thermo-diffraction patterns (Fig. 3). At the lowest temperature of 400°C the ZrO_2 crystal size ranged between 25 Å and 75 Å. In this case, the crystal size was basically identical in both systems, as it could be expected, because the thermo-diffraction pattern was obtained from the sample previously heated at 400°C. Nevertheless, although the crystal size distribution increased in both systems, the crystal sizes measured in the standard XRD patterns were larger than those obtained on the thermo-diffraction patterns. For example, samples treated at 800°C increased their sizes on average to 90 Å and 130 Å in the thermo-diffraction and standard patterns respectively. At 900°C, while the thermo-diffraction patterns produced a bimodal crystal size distribution with peaks at around 100 Å and 212 Å, the standard diffraction pattern produced only a crystal size distribution

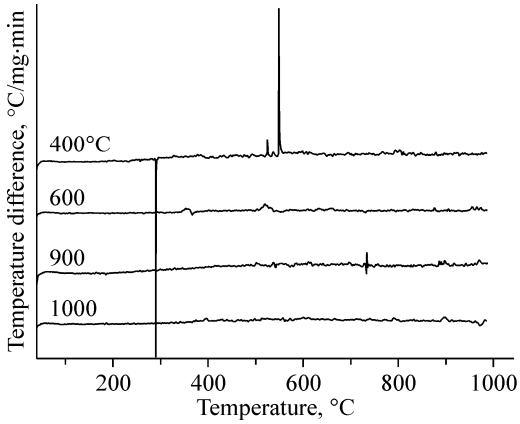

Fig. 4. Differential thermal analyses of the $MgO–ZrO_2$ samples previously heat-treated at different temperatures.

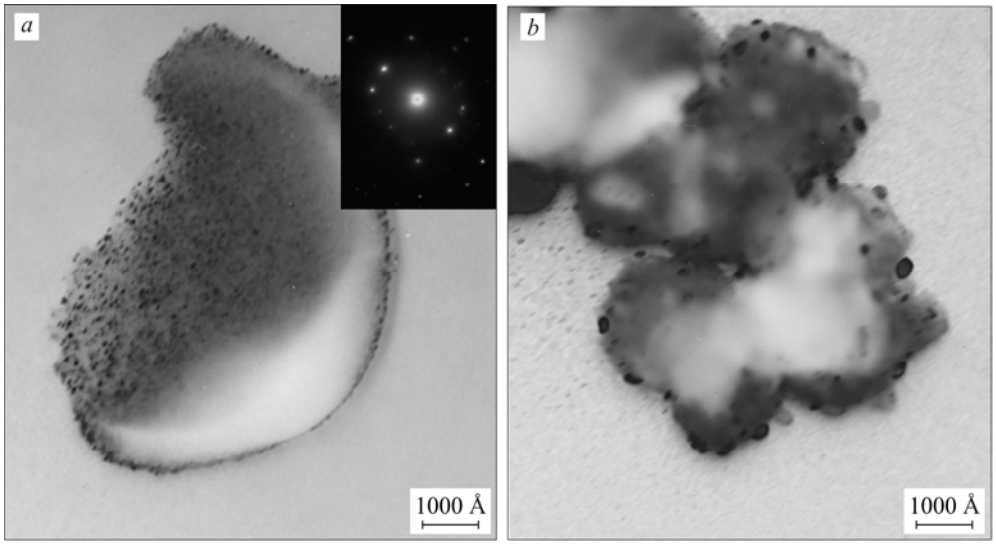

Fig. 5. Bright field images and electron diffraction pattern from the sample $MgO–ZrO_2$ heat-treated at 400°C (*a*) and 900°C (*b*).

centered at 450 Å. Finally, at 1000°C both samples presented large crystals of 215 Å (thermo-diffraction) and 2000 Å (standard diffraction), while smaller crystallites disappeared. Crystal size distribution differences obtained from the standard and thermo-diffraction patterns may be attributed to different heat-treatments. While the standard diffraction samples were heat-treated at each temperature for eight hours, thermo-diffraction was obtained in-situ, without any further treatment.

These results were in agreement with the DTA analyses (Fig. 4). The sample previously treated at 400°C exhibited two peaks. The first one was an intense endothermic peak at 289°C, which should correspond to the thermal decomposition of magnesium nitrate residues. However, the most interesting peak appeared at 550°C. This exothermic peak fits very well with the transition between cubic and tetragonal ZrO_2 phases [27]. Hence, this result strongly suggests the presence of the ZrO_2 cubic phase at low temperatures. The other samples did not present any evident peak, which shows that the cubic phase already disappeared. This analysis confirms the previous XRD observations, where the existence of the ZrO_2 cubic phase was presupposed, which converts into the tetragonal and monoclinic phases as a function of temperature.

Fig. 5 shows the TEM bright field images of the $MgO–ZrO_2$ samples heat-treated at 400°C and 900°C. Again, two different types of particles appear. The large ones correspond to MgO and the small ones to ZrO_2 particles. The ZrO_2 particles

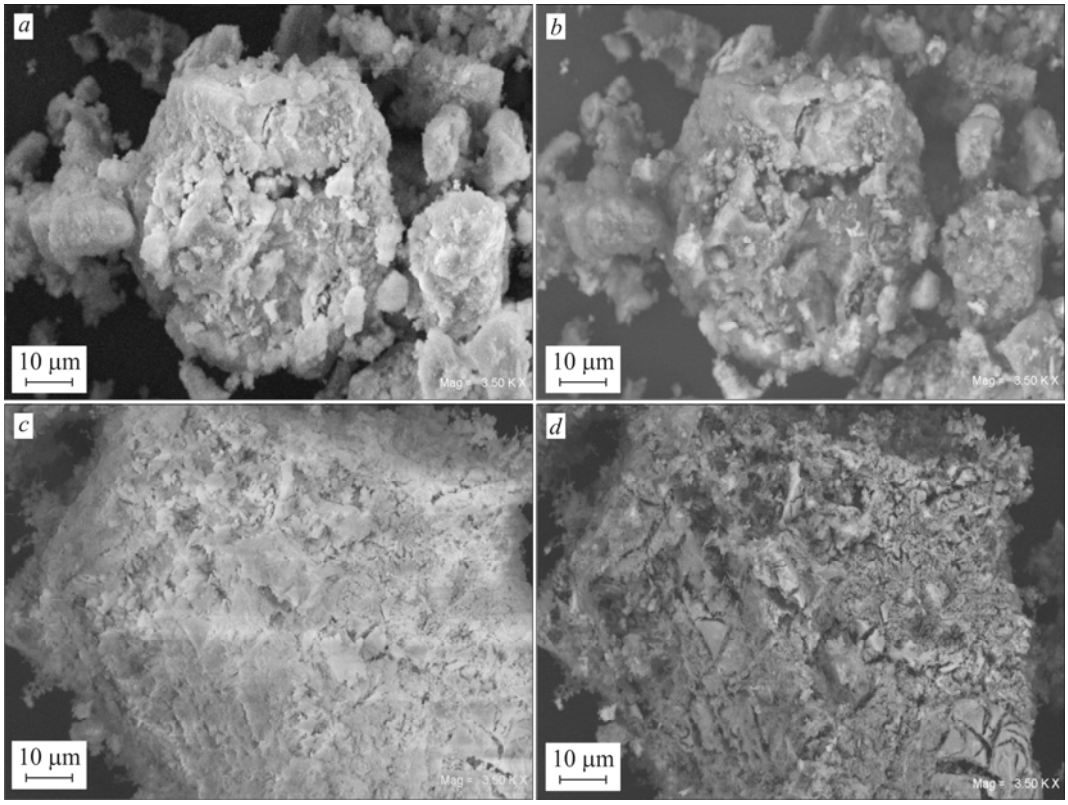

Fig. 6. SEM images of the samples heat-treated at 400°C (*a*) secondary electrons, (*b*) backscattered electrons and 900°C (*c*) secondary electrons and (*d*) backscattered electrons.

grew from *ca*. 100 Å (400°C) up to 500 Å (900°C). From these images it can be concluded that the ZrO_2 particles are supported on MgO. However, since the amount of ZrO_2 is as high as the MgO amount, very small particles of ZrO_2 must be present as well, either as supported particles or as occluded ones.

Electron diffraction patterns of the small particles of the sample treated at 400°C were obtained, but since the particles are very small and the MgO phase was present all around, it was not possible to obtain an ideal electron diffraction pattern. Nevertheless, several diffraction spots on these patterns could be, again, correlated to the cubic ZrO_2 phase.

SEM analyses of different samples are shown in Fig. 6, where some microstructural changes as a function of the calcination temperature are evident. In the sample heat-treated at 400°C (Fig. 6*a*), two different kinds of particles were evidenced; on the one hand, large agglomerates (60-70 μm) presenting a non-homogeneous morphology and, on the other hand, smaller particles (4-5 μm) distributed on top of the large ones. The same image, but obtained with backscattered electrons, showed that the composition of the two types of particles is different as well, as shown by the differences in contrast Fig. 6*b*, which arises from the differences in the mean atomic number of ZrO_2 (18.66) and MgO (10) [28]. In this case, ZrO_2 is the lighter phase and MgO is the darker phase. Hence, the surface of the particles is mainly constituted by the MgO matrix where some ZrO_2 tiny particles are shown up.

Nevertheless, at higher temperatures both the morphology and phase distribution changed in the samples. While the large particles grew to 130-140 μm and seemed to become denser, the small particles tended to disappear (Fig. 6*c* and *d*). In fact, in some regions it looked as if the ZrO_2 small particles wetted the surface of the MgO particles because a more brilliant phase seemed to spread all over the MgO particles (Fig. 6*d*).

All the previous results suggested the densification of the material with temperature. This information was confirmed by the N_2 adsorption analysis (Fig. 7). All the samples presented isotherms of type II exhibiting narrow H3 type hysteresis loops, according to the IUPAC classification. This behavior corresponds to non-porous materials, and it is typically

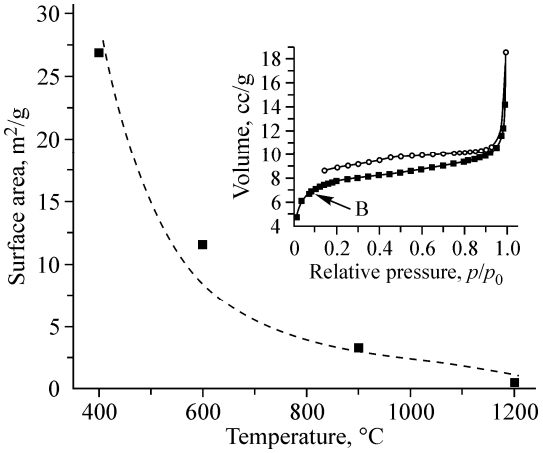

Fig. 7. Decrement trend obtained for the BET surface areas as a function of the temperature. The inset shows the typical nitrogen isotherm obtained for the $MgO–ZrO_2$ sample (sample showed 400°C).

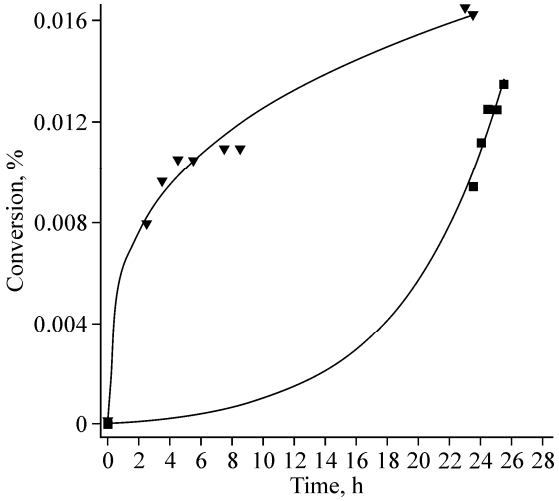

Fig. 8. Catalytic conversion, of acetone to diacetone alcohol, using the $MgO–ZrO_2$ samples heat treated at 600°C and 900°C.

differentiated from the point B, which indicates the saturation of the first adsorption monolayer. Additionally, as a consequence of the temperature, the surface area values diminished from 26.9 m^2/g to 0.4 m^2/g for the samples heat-treated at 400°C and 1200°C respectively.

Finally, the samples were evaluated as catalysts using the following aldolic condensation reaction of acetone (see reaction 1), which produces di-acetone alcohol (DAA). The $MgO–ZrO_2$ samples heat-treated at 400°C, 1000°C, and 1200°C did not show any kind of catalytic activity. On the other hand, the samples heat-treated at 600°C and 900°C were active as catalysts for this reaction (Fig. 8). It seems that although both samples tend to similar conversion factors after 24 h, the sample heat-treated at 900°C produces a faster kinetic reaction evolution in the first hours of the reaction.

DISCUSSION

Summarizing, from the XRD data different composites were identified as a function of heat-treatment. MgO was obtained in all cases, and its crystallinity did not change as a function of temperature. However, it is important to mention that the MgO crystalline phase is not observed below 800°C in $MgO–ZrO_2$ synthesized via other techniques such as the citrate gel process [23]. Conversely, different polymorphs of ZrO_2 were obtained as a function of temperature. At low temperatures, it was not possible to distinguish between cubic and tetragonal ZrO_2 phases because the XRD peaks were very broad, and both phases present peaks in almost the same Bragg angles. When temperature was increased to 800°C or higher, the tetragonal phase was definitively identified. Finally, at the highest temperatures (1000-1200°C) the tetragonal phase converted into the monoclinic phase. An important observation is that from the other reports, a complete transformation from tetragonal to monoclinic polymorphs of zirconia occurs at temperatures of 1000°C and solid solutions containing ≤60% mol MgO as stabilizer [23]. Nevertheless, in these materials only about 44% of the tetragonal phase was transformed to the monoclinic phase after heat treatment at 900°C and about 72% at 1200°C. The above suggests a better stabilization for zirconia in this composite. Additionally, the transition from cubic to tetragonal ZrO_2 phase was confirmed by the DTA analysis. All these measurements are in agreement with the transmission electron microscopy results. This technique shows that ZrO_2 particles are located in the bulk and distributed all over the surface of larger MgO particles. Additionally, it was observed that the particle surface became more homogeneous. This feature was confirmed by N_2 adsorption as the surface area was significantly reduced.

According to all these results, the cubic and tetragonal ZrO_2 phases are stabilized through two different mechanisms: constriction and doping. The constriction mechanism is proposed by the TEM images, where some ZrO_2 particles seem to be immersed into the MgO matrix, while the doping mechanism was shown by a shift of the ZrO_2 interplanar distances observed by XRD. Additionally, the use of zirconium acetate as Zr precursor may have contributed to the cubic and tetragonal ZrO_2 formation. It is well known that cubic and tetragonal ZrO_2 stabilization occurs with the formation of oxygen vacancies. The ZrO_2 synthesis through a normal combustion of one mol of zirconium acetate needs the presence of eight moles of O_2. Hence, since the zirconium phase, after the precipitation process, seems to be occluded into the magnesium oxide network, it might have inhibited the correct oxygenation of ZrO_2 crystals, promoting the presence of oxygen vacancies.

These results are in agreement with the previous reports that establish the critical crystallite size in which cubic and tetragonal ZrO_2, pure or mixed with other oxides, are present at room temperature [22, 29, 30]. Still, while some authors report the cubic ZrO_2 phase existence at room temperature [26, 31, 32], the others claim that it cannot be true [22]. Those who support the existence of cubic ZrO_2 reported that the critical crystal size must have been 50-100 Å. Instead, there is a general agreement on the existence of tetragonal ZrO_2 at room temperature, pure and as a composite. In this case, it has been reported that the maximum crystallite size corresponds to 300 Å for pure tetragonal ZrO_2 and to 480-500 Å as a composite [29, 30]. Nevertheless, it has to be pointed out that the presence of tetragonal and/or cubic ZrO_2 does not limit the formation of monoclinic ZrO_2 nanocrystals [32].

It should be noted that ZrO_2 cubic and tetragonal phases supported on MgO are in close agreement with the literature data, including the presence of the cubic ZrO_2 phase at low temperatures. Therefore, the stabilization and evolution of ZrO_2 polymorphs, from cubic to tetragonal and monoclinic, must be due to the crystallite size and sintering effects caused by heat-treatment. At low temperatures ZrO_2 presents a cubic structure that converts to tetragonal ZrO_2 when temperature is increased. The ZrO_2 transformation from cubic to tetragonal is mainly induced by an increase in the crystallite size. In this case, the critical crystallite size, in which ZrO_2 transformed from cubic to tetragonal, was found to be around 100-110 Å. Finally, at higher temperatures, the monoclinic phase is obtained, and it should happen again through a crystallite size evolution, since the critical size reported for the tetragonal phase is 500 Å in a composite. Then, changes in the crystallite size distribution values observed at high temperatures correspond to the growth of crystallites, which are involved later in the transformation to the monoclinic phase, occurring upon cooling.

The chemical behavior and the observed differences may be attributed to the differences in the starting compounds: $Mg(NO_3)_2$ and ZrO_2. Initially, ZrO_2 precipitates forming small particles. Then, $Mg(NO_3)_2$ covers the ZrO_2 particles, once the solution becomes oversaturated and dried. Thermal treatment decomposes $Mg(NO_3)_2$, and then MgO forms as a matrix encapsulating the ZrO_2 particles.

The catalytic performance of the MgO–ZrO_2 conversion of acetone to DAA is favored by basic sites, which in this case, are provided by MgO. In a previous work with a MgO–Al_2O_3 composite, the catalytic activity was attributed to the surface distribution of Mg. As Lewis acidity increased, water formed inhibiting catalytic performance [33]. Zirconium did not behave as aluminum. Initially, magnesium oxide contains some zirconium atoms incorporated into the magnesium oxide lattice generating structural defects whose electronic effect is such that acetone conversion is inhibited. With temperature, those zirconium atoms migrate and incorporate into ZrO_2 particles. Then, the MgO surface becomes basic and catalytically active. Such a mechanism is confirmed by the inactivity observed with the high-temperature treated samples. The amount of surface segregated ZrO_2 is such that it completely covers the MgO active surface. The conversion curve presented by the MgO–ZrO_2 sample treated at 900°C shows a high activity at short times, which continues up to 26 h reaching the values as high as 0.017%, which is lower by 50% as compared to the MgO–Al_2O_3 system [33]. The acid-base MgO–TiO_2, instead, decomposes diacetone alcohol to acetone [9]. The MgO–ZrO_2 sample treated at 600°C has a very low initial activity, which increased after 24 h up to 0.014%. The differences observed can be attributed to two different factors. The presence of different ZrO_2 phases: cubic ZrO_2 is present on the sample treated at 600°C, which is mostly acid. These particles should initially promote the acetone acid conversion to water; water then poisons the ZrO_2 surface after some time. At that point, acetone is free to react on the MgO basic surface to produce DAA, as shown by the curve. It should be emphasized that the

sample treated at 900 °C contains tetragonal ZrO_2, which is not as acid as the cubic phase. Thus, acetone is able to react on the MgO surface. Although in this case only a basic reaction was tested, the synthesized composites are acid-base catalysts, whose activity would be modulated depending on Zr segregation in MgO–ZrO_2 composites.

CONCLUSIONS

The synthesis of the zirconia-magnesia composite system was carried out by the precipitation technique and heat treatment at different temperatures. The results show that different zirconia phases are obtained as a function of heat-treatments. At low temperatures cubic zirconia was stabilized by constriction and doping in magnesium doped oxide. If temperature is increased, cubic zirconia transforms to tetragonal and monoclinic phases subsequently. In the tetragonal case, although it was stabilized by constriction and doping, the main contribution seems to be the doping effect.

The acid-base character of the prepared composites was tested by the acetone conversion to diacetone alcohol. Acetone reacts to produce either water on acid sites or diacetone alcohol on basic sites; these two reactions are competitive, and depending on the MgO surface purity and ZrO_2 acidity, the reaction orients towards water or diacetone alcohol.

Authors thank L. Baños, A. Tejeda, C. Flores, and E. Fregoso for technical help, and CONACYT as well as PAPIIT-UNAM (IN100609) for financial support.

REFERENCES

1. O. V. Karban, O. L. Khasanov, and O. M. Kanunnikova, *J. Struct. Chem*., **45**, S149-S155 (2004).
2. R. Mucillo, E. N. S. Mucillo, and N. H. Saito, *Mater. Lett*., **34**, 128 (1998).
3. A. C. Geiculescu and H. G. Spencer, *J. Sol-Gel Sci. Tech*., **17**, 25 (2000).
4. M. F. Hassan and M. Gupta, *J. Composite Mater*., **41**, 2533 (2007).
5. A. Kah-Soh, D. Fang, and Z. X. Dong, *J. Composite Mater*., **38**, 227 (2004).
6. D. Ciuparu, A. Ensuque, and F. Bozon-Verduraz, *Appl. Catal. A*, **326**, 130 (2007).
7. M. A. Aramendia, V. Boráu, C. Jiménez, et al., *Colloid Surf. A: Physicochem. Eng. Aspects*, **234**, 17 (2004).
8. N. O. Lemcoff and R. E. Cunningham, *J. Catal*., **23**, 81 (1971).
9. K. Tanabe, H. Hattori, T. Sumiyoshi, et al., *J. Catal*., **53**, 1 (1978).
10. V. K. Díez, C. R. Apesteguía, and J. I. Di Cosimo, *J. Catal*., **240**, 235 (2006).
11. G. Carta, N. E. Habra, G. Rossetto, et al., *Surf. Coat. Tech*., **201**, 9289 (2007).
12. I. Taymaz, K. Fakir, and A. Mimaroglu, *Surf. Coat. Tech*., **200**, 1182 (2005).
13. A. S. Demirkiran and E. Avici, *Surf. Coat. Tech*., **116-119**, 292 (1999).
14. C. Tekmen, I. Ozdemir, and C. Celik, *Surf. Coat. Tech*., **174/175**, 1101 (2003).
15. V. M. Zainullina, V. P. Zhukov, V. M. Zhukovskii, et al., *J. Struct. Chem*., **41**, 229-239 (2000).
16. A. H. Heder, N. Claussen, W. M. Priven, et al., *J. Am. Ceram. Soc*., **65**, 642 (1982).
17. R. Srinivasan, C. R. Hubbard, O. V. Cavin, et al., *Chem. Mater*., **5**, 27 (1993).
18. R. D. Sisson Jr. and B. M. Smyser, *Nanostruct. Mater*., **10**, 829 (1998).
19. T. Czeppe, P. Zieba, and A. Pawlowski, *J. Europ. Ceram. Soc*., **22**, 35 (2002).
20. F. Monte, W. Larsen, and J. D. Mackenzie, *J. Am. Ceram. Soc*., **83**, 628 (2000).
21. R. Piticescu, C. Monty, and D. Millers, *Sensors and Actuators B*, **109**, 102 (2005).
22. D. G. Lamas, A. M. Rosso, M. Suarez-Anzorena, et al., *Scripta Materialia*, **55**, 553 (2006).
23. H. Gocmez and H. Fujimori, *Mater. Sci. Eng. B*, **148**, 226 (2008).
24. B. T. Lee, K. Hiraga, D. Shindo, et al., *J. Mater. Sci*., **29**, 959 (1994).
25. R. D. Bonetto, H. R. Viturro, and A. G. Alvarez, *J. Appl. Cryst*., **23**, 136 (1990).
26. D. Sarkar, S. Adak, and N. K. Mitra, *Composites: Part A*, **38**, 124 (2007).

27. S. Roy and J. Ghose, *Mater. Res. Bull*., **35**, 1195 (2000).
28. J. I. Goldstein, D. E. Newbury, P. Echlin, et al. *Scanning Electron Microscopy and X-ray Microanalysis*, Plenum, New York (1981), pp. 75-77.
29. F. Monte, W. Larsen, and J. D. Mackenzie, *J. Am. Ceram. Soc*., **83**, 628 (2000).
30. J. Ortiz-Landeros, M. E. Contreras, and H. Pfeiffer, *J. Porous Mater*., **16**, 473 (2009).
31. G. Stefanic, S. Popovic, and S. Music, *Thermochim. Acta*, **303**, 31 (1997).
32. D. A. Zyuzin, E. M. Moroz, A. S. Ivanova, et al., *Kinet. Catal*., **45**, 780 (2004).
33. A. E. Sommer, J. A. Rivera, G. Fetter, et al., *Rev. Mex. Fis*., **5**, 245 (2006).